ACS Catalysis

Research Article

pubs.acs.org/acscatalysis

Comparative Investigation of Benzene Steam Reforming over Spinel Supported Rh and Ir Catalysts

Donghai Mei,*[,†] Vanessa M. Lebarbier,[‡] Roger Rousseau,[†] Vassiliki-Alexandra Glezakou,[†] Karl O. Albrecht,[‡] Libor Kovarik,[§] Matt Flake,[‡] and Robert A. Dagle*[,‡]

[†]Fundamental and Computational Sciences Directorate, Institute for Integrated Catalysis, Pacific Northwest National Laboratory, Richland, Washington 99352, United States

[‡]Energy and Environmental Directorate, Institute for Integrated Catalysis, Pacific Northwest National Laboratory, Richland, Washington 99352, United States

[§]The William R. Wiley Environmental Molecular Sciences Laboratory, Pacific Northwest National Laboratory Richland, Washington 99352, United States

ABSTRACT: In a combined experimental and first-principles density functional theory (DFT) study, benzene steam reforming (BSR) over $MgAl_2O_4$-supported Rh and Ir catalysts was investigated. Experimentally, it has been found that both highly dispersed Rh and Ir clusters (1−2 nm) on the spinel (e.g., $MgAl_2O_4$) support are stable during the BSR in the temperature range of 700−850 °C. Compared to the $Ir/MgAl_2O_4$ catalyst, the $Rh/MgAl_2O_4$ catalyst is more active with higher benzene turnover frequency and conversion. At steam conditions with the molar steam-to-carbon ratio >12, the benzene conversion is only a weak function of the H_2O concentration in the feed. This suggests that the initial benzene decomposition step, rather than the benzene adsorption, is most likely the rate-determining step in BSR over supported Rh and Ir catalysts. To understand the differences between the two catalysts, we followed with a comparative DFT study of initial benzene decomposition pathways over two representative model systems for each supported metal (Rh and Ir) catalysts. A periodic terrace (111) surface and an amorphous 50-atom metal cluster with a diameter of 1.0 nm were used to represent the two supported model catalysts under low and high dispersion conditions. Our DFT results show that the decreasing catalyst particle size enhances the benzene decomposition on supported Rh catalysts by lowering both C−C and C−H bond scission. The activation barriers of the C−C and the C−H bond scission decrease from 1.60 and 1.61 eV on the Rh(111) surface to 1.34 and 1.26 eV on the Rh_{50} cluster. For supported Ir catalysts, the decreasing particle size only affects the C−C scission. The activation barrier of the C−C scission of benzene decreases from 1.60 eV on the Ir(111) surface to 1.35 eV on the Ir_{50} cluster while the barriers of the C−H scission are practically the same. The experimentally measured higher BSR activity on the supported highly dispersed Rh catalyst can be rationalized by the thermodynamic limitation for the very first C−C bond scission of benzene on the small Ir_{50} catalyst. The C−C bond scission of benzene on the small Ir_{50} catalyst is highly endothermic although the barrier is competitive with those of both the C−C and the C−H bond-breaking on the small Rh_{50} catalyst. The calculations also imply that, for the supported Rh catalysts, the C−C and C−H bond scissions are competitive, independent of the Rh cluster sizes. After the initial dissociation step via either the C−C or the C−H bond scission, the C−H bond breaking seems to be more favorable rather than the C−C bond breaking on the larger Rh terrace surface.

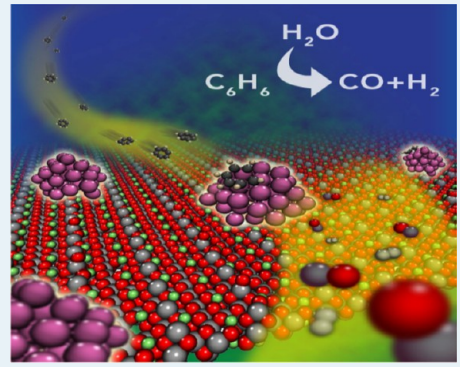

KEYWORDS: *benzene, steam reforming, density functional theory, rhodium, iridium, reaction pathways*

1. INTRODUCTION

With decreasing fossil fuel supplies and increasing energy demand, the renewable energy production from biomass resources has received substantial attention in recent years.[1] Among several developing biomass utilization technologies, biomass gasification is one of major routes in the conversion of biomass to clean syngas and fuel gases.[2,3] The typical products from biomass gasification process consist of H_2, CO, CO_2, light hydrocarbons and large amounts of organic impurities. These organic impurities, generally referred to as tars, include a significant fraction of polycyclic aromatic hydrocarbons, such as benzene, toluene, and naphthalene, which can cause a severe operation problem by plugging reactor channels and deactivating the catalyst.[2] Therefore, the effective removal or conversion of tars has become one of most important technical challenges (barriers) in large-scale biomass gasification technologies.[4] Although both physical separation and catalytic cracking measures can be used for the tar removal purpose, the catalytic

Received: January 21, 2013
Revised: April 1, 2013
Published: April 16, 2013

   dx.doi.org/10.1021/cs4000427 | ACS Catal. 2013, 3, 1133−1143

steam reforming method is more effective and economically appealing.[3] Currently, commercial Ni-based catalysts are widely studied for the steam reforming of biomass tars.[3−5] However, nickel is well-known to be prone to deactivation from coke.[3] Thus, aside from Ni, group VIII metals have been evaluated. For example, Tomishige suggested the following activity order for steam reforming of biomass-derived tars: Rh > Pt > Ni > Pd > Ru.[6] Further experimental measurements indicate that Rh-based catalysts suffer from less coking compared to other group VIII metals.[6,7] By using benzene as a model tar compound, Colby et al. recently studied benzene steam reforming (BSR) over Rh/α-Al_2O_3 and Rh−Ce/α-Al_2O_3 catalysts in the temperature range of 700−900 °C.[8] They found that promotion of Rh-based catalysts with Ce leads to an increase of the Rh dispersion and better stability for BSR. In addition to the strong temperature and steam/carbon (S/C) ratio effects, they also observed that the cofed CO_2, H_2, and CO had different effects on the benzene conversion. Although many experimental studies on the macroscopic activity of tar steam reforming on various catalysts have been reported, very little molecular level knowledge is available, especially on how and where those polycyclic aromatic compounds break up into the small hydrocarbon fragments on the catalyst surface.

The overall stoichiometric BSR reaction can be written as follows:

$$C_6H_6 + 6H_2O \rightarrow 6CO + 9H_2 \quad \Delta G^\circ(1173\ K) = -490\ KJ/mol \tag{1}$$

It has been postulated that the adsorbed benzene undergoes a stepwise decomposition into hydrocarbon intermediates C_xH_y via either a C−C or a C−H bond-breaking steps.[4] C_xH_y species will irreversibly convert into the final products, CO, CO_2, H_2, and CH_4 (eq 2-eq 4). Water-gas shift (eq 3) and methane steam reforming (eq 4) are commonly accompanying reactions during BSR conversion:

$$C_xH_y + xH_2O \rightarrow xCO + (x + y/2)H_2 \tag{2}$$

$$CO + H_2O \rightarrow CO_2 + H_2 \tag{3}$$

$$CH_4 + H_2O \rightarrow CO + 3H_2 \tag{4}$$

Simell et al. proposed a Langmuir−Hinshelwood type mechanistic model describing the benzene decomposition over a dolomite catalyst in the presence of CO_2.[9] In their model, they assumed benzene adsorption to be the rate-determining step. The adsorbed benzene can subsequently undergo the steam reforming to hydrocarbons (ethane) as proposed by Rostrup−Nielsen.[10] Colby et al. suggested that benzene adsorbed on Rh-based catalyst would be rapidly and completely dehydrogenated into atomic C and H via C−C and C−H bond cleavages.[8] The coking probability depends on how these strongly bonded C species can be effectively removed in the form of CO after reaction with hydroxyl groups from H_2O dissociation on the support. On the basis of this reaction scenario, it is reasonable to assume that the initial benzene decomposition steps involving the first C−C bond breaking and ring-opening steps will be the rate-determining steps.

Thermal decomposition and oxidation of benzene over single crystal Rh(111) and Ir(111) surfaces have been studied using temperature programmed desorption (TPD), high-resolution electron energy loss spectroscopy (HREELS) and low-energy electron diffraction (LEED) techniques under UHV condition.[11,12] Instead of the initial C−H bond-breaking that was observed on Pt(111) surface,[13] Koel et al.[11] proposed that the decomposition of benzene on the Rh(111) surface begins with the C−C bond-breaking at 400 K. The adsorbed benzene breaks up into three acetylene species that will further decompose into a mixture of CH and C_2H species with CH/C_2H ratio ∼0.4. A similar study of benzene adsorption and oxidation on Ir(111) by Weststrate et al. suggested that two possible benzene decomposition mechanisms exist.[12] In the first mechanism, about one-third of the adsorbed benzene decomposes via the C−C bond-breaking forming six CH species, while the other two-thirds decompose via C−H fragmentation, forming C_6H_y, where $y < 6$. The second benzene decomposition route can further break up the C_6 backbone to generate C_xH_y ($x < 6$) and CH.

The interaction of benzene with transition metals and its hydrogenation over metal surfaces has also been studied with first principles density functional theory (DFT) calculations.[14−20] It has been found that benzene preferentially adsorbs on the metal surface with the ring parallel to the surface plane. Compared to many DFT studies of benzene hydrogenation,[17,19−21] theoretical studies of benzene dehydrogenation are rare.[22,23] Gao et al. found two parallel reaction pathways of benzene dehydrogenation on Pt(111) leading to the C_6H_3 species with similar reaction energy barriers.[22] However, they did not consider the C−C bond breaking in their calculations. To the best of our knowledge, there has been no modeling of benzene decomposition mechanism on metal catalysts in the literatures to date.

In the present work, the activity for BSR was tested over a 5%Rh/$MgAl_2O_4$ catalyst and a 5%Ir/$MgAl_2O_4$ catalyst in the temperature range of 700−850 °C where both catalysts were found to be highly active. Higher turnover rates and conversion were observed for the supported Rh catalyst. These Rh and Ir catalysts were also found to be active and stable when evaluated under model gasifier-derived syngas feed, which included benzene and other tar-representative surrogates. Thus, they are promising catalysts for use in a catalytic conditioning process for biomass-derived syngas. To gain fundamental insights into the reaction mechanism of benzene decomposition and compare the catalytic performance of BSR reaction over supported Rh and Ir catalysts, a combined theoretical study was also performed. In particular, the particle size effects on the reactivity were investigated using the (111) surface facet of Rh and Ir, as well as 50-metal atom (∼1 nm) clusters, Rh_{50} and Ir_{50}. These two model systems represent the potential reactivity of the two metals toward benzene, for both large and small nanoparticles. The initial decomposition steps of benzene via both C−C and C−H bond breaking on the above four model catalysts systems were explored using first-principles DFT calculations for the first time. These DFT calculations not only elucidate the experimental observations presented here, but also provide us with the general picture of benzene decomposition over supported metal catalysts at the molecular level.

2. EXPERIMENTAL SECTION

2.1. Catalyst Preparation. Supported Rh and Ir catalysts were prepared by incipient wetness impregnation of $MgAl_2O_4$ (Sasol Puralox 30/140) calcined at 500 °C with solutions of rhodium and iridium nitrate (Sigma Aldrich 99%) dissolved in deionized water. After impregnation, the catalysts were dried at 110 °C for 8 h and calcined under air at 500 °C for 3 h. The

dx.doi.org/10.1021/cs4000427 | ACS Catal. 2013, 3, 1133−1143

metal loading was 5 wt % for both catalysts designated as 5% $Rh/MgAl_2O_4$ and 5%$Ir/MgAl_2O_4$.

2.2. STEM Analysis. Scanning Transmission Electron Microscopy (STEM) measurements were conducted with a FEI Titan 80−300 operated at 300 kV. The FEI Titan is equipped with CEOS GmbH double-hexapole aberration corrector for the probe-forming lens, which allows imaging with ∼0.1 nm resolution in scanning transmission electron microscopy (STEM) mode. The STEM images were acquired on High Angle Annular Dark Field (HAADF) with inner collection angle of 52 mrad. In general, the TEM sample preparation involved mounting of powder samples on copper grids covered with lacey carbon support films and immediate loading them into the TEM airlock to minimize an exposure to atmospheric O_2.

STEM images were used to determine average Rh and Ir particle sizes after reduction at 850 °C. Approximately 150 clusters were counted in determining the average size. Metal dispersion was calculated assuming hemispherical geometry using the equation, $D = 1/d$, where D is the fractional dispersion and d is the cluster diameter (nm).[24,25] Dispersion calculations were used to calculate moles of accessible metal sites. Benzene turnover was calculated as moles of benzene converted per moles of accessible metal sites per min (mol/mol/min). Resulting metal cluster size, dispersion, and benzene turnover details are given in Table 1.

Table 1. Particle Sizes, Dispersion, and Benzene Turnover Frequencies [T = 700 °C, P = 1 atm, GHSV = 890 000 h^{-1}; Feed = 64.9% N_2, 34.6% H_2O, and 0.5% C_6H_6 (molar)] for the 5% $Rh/MgAl_2O_4$ Catalyst and the 5% $Ir/MgAl_2O_4$ Catalyst

catalyst	metal cluster sizes (nm)	metal dispersion (%)	benzene turnover rate (mol/mol/min)
5%$Rh/MgAl_2O_4$	2.1 (±0.5)	48	74
5%$Ir/MgAl_2O_4$	1.0 (±0.3)	100	42

2.3. Reactivity. Catalytic activity tests for benzene steam reforming were conducted in a 1/4 in. OD (ID = 4.57 mm) fixed-bed inconel reactor. A K-type thermocouple was placed in the reactor for measurement of the catalyst bed temperature. Heat and mass transfer effects were minimized by using relatively small catalyst particle sizes (i.e., 60−100 mesh), diluting 12 mg of catalyst with 120 mg of α-Al_2O_3, and utilizing high linear flow velocities. The diluted catalyst was loaded between two layers of quartz wool. A "blank" experiment was conducted using α-Al_2O_3. For each test, the catalysts were first reduced in situ at 850 °C for 2 h, using a 10 mol % H_2/He gas mixture. Then, prepurified nitrogen was introduced into the system using a Brooks mass flow controller (5850E series) along with water and benzene. Note that water was fed into the system using a microchannel vaporizer and an HPLC syringe pump (Accuflow Series III). Benzene was fed to the system using a microchannel vaporizer and an ISCO syringe pump. The effects of H_2O and benzene feed compositions on benzene conversion were measured over a wide range of reactant concentrations at 700 °C, atmospheric pressure, and GHSV = 220 000 h^{-1} (calculated including both diluent and catalyst volume). Gas-hourly space-velocity was kept constant by adjusting nitrogen dilution. Benzene turnover rates were measured at 700 °C, atmospheric pressure, GHSV = 890 000 h^{-1} and using a feed mixture containing 0.5% benzene, 34.6% H_2O, and 64.9% N_2 (molar), resulting in a molar steam-to-carbon ratio (S/C) equivalent of 12. Gaseous effluent was analyzed using an Inficon micro GC (Model 3000A) equipped with MS-5A, Plot U, and OV-1 columns and a thermal conductivity detector (TCD).

3. COMPUTATIONAL DETAILS

For large supported metal catalysts, the most exposed surface consists predominantly of (111) facets. Hence our model for these larger particles consists of periodical Rh(111) and Ir(111) surface slabs with a $p(3 \times 3)$ supercell of four atomic layers in thickness. A 15 Å vacuum layer was inserted between the neighboring (111) surface slabs in the z direction to avoid unphysical interaction between two surface slabs. The periodic DFT slab calculations were performed using the Vienna Ab-initio Simulation Package (VASP).[26−28] The core and valence electrons were represented by the projector augmented wave (PAW) method with a kinetic cutoff energy of 400 eV.[29,30] The generalized gradient approximation (GGA) combined with the Perdew−Burke−Ernzerhof (PBE) functional[31] describing the exchange correlation functional was used in the calculations. To ensure the accuracy of calculations, the effects of the slab thickness (up to six atomic layers) and different Monkhorst−Pack (MP) mesh sampling ranging from (2 × 2 × 1) to (4 × 4 × 1) were tested. A (3 × 3 × 1) k-point sampling schedule combined with the surface slab of four atomic layers was found to be converged within the energy of 0.03 eV. After the slab optimizations, the adsorbates and the metal atoms of the top two surface layers were allowed to relax while the metal atoms of the bottom two layers of the (111) surface slabs were fixed. The ground-state atomic geometries of clean surfaces alone and with the adsorbed systems were obtained by minimizing the forces on each atom to below 0.03 eV/Å. A van der Waals correction[32] was implemented in all calculations of this work. The effect of the zero point energy correction (ZPEC) on the reaction energetics was checked by the C−H bond scission of benzene on Rh(111). We found that the variations in the relative energetics with/without the ZPEC in this reaction path were relatively small (<0.1 eV). Therefore, we neglected the ZPEC in our calculations.

We believe that the spinel support plays an important role in controlling metal particle size, and it is not involved in the reaction. Therefore, to simplify the computation, we eliminated the spinel support in this set of calculations. Fifty atom clusters (Rh_{50} and Ir_{50}, with ∼1 nm diameter) were used to model the small, finite-size supported metal particles. Each of the model metal clusters was obtained with the standard simulated annealing method using ab initio molecular dynamics simulations and a cubic box of 20 × 20 × 20 $Å^3$. Each cluster was initially equilibrated at T = 1000 K for a duration of 2−3 ps, followed by equilibration within the canonical ensemble at T = 800 K for 20 ps and cooled to T = 0 K over the duration of ∼1−2 ps to obtain the final cluster structures. We believe these fully equilibrated clusters, which are different from the well-defined cluster model, such as octahedron and cuboctahedron, are more realistic for the representation of the spinel-supported metal catalysts under high temperature and high dispersion condition. All calculations on the Rh_{50} and Ir_{50} clusters were carried out using the CP2K package.[33,34] The GGA-PBE functional and the pseudopotentials of Geodecker, Teter, and Hutter and a cutoff energy of 320 Ry of the auxiliary plane wave

dx.doi.org/10.1021/cs4000427 | ACS Catal. 2013, 3, 1133−1143

basis were used in the calculations. The Broyden–Fletcher–Goldfarb–Shanno (BFGS) algorithm, allowing for a rapid self-consistency, with the SCF convergence criteria of 1.0×10^{-6} au was also used.

The transition states of initial benzene decomposition steps including both C–H and C–C bond scissions on periodic (111) surfaces and 50-atoms clusters were searched using the minimum-mode following dimer method,[35] as implemented in VASP. The advantage of the dimer method is the ability to explore various unbiased reaction pathways without prior knowledge of the possible final state (product). We have successfully used this method to map out the reaction landscapes of various systems in recent studies.[36−40] In the current study, the dimer separation distance was set at 0.0l Å and the tolerance for the convergence to the transition state was such that the force on each atom was less than 0.03 eV/Å.[35]

The adsorption energies $E_{A_{ads}}$ of benzene and its dissociation derivatives on the cluster and the (111) surface are calculated as

$$E_{A_{ads}} = E_{A+S} - E_S - E_A \quad (5)$$

where E_{A+S} is the total energy of the adsorbate(s) on the cluster or the surface, E_S is the total energy of the bare cluster or the (111) surface, and E_A is the total energy of the adsorbate molecule (or radical) in vacuum with the same simulation box size.

4. RESULTS AND DISCUSSION

4.1. Experimental BSR on Supported Rh and Ir Catalysts. *4.1.1. Experimental Catalysts Characterization.* The 5% Ir/$MgAl_2O_4$ and 5% Rh/$MgAl_2O_4$ catalysts were analyzed using STEM after reduction at 850 °C (2 h, 10% H_2/He) in order to determine cluster sizes and metal dispersion. Representative STEM images are shown in Figure 1a for 5% Ir/$MgAl_2O_4$ and Figure 1b for 5% Rh/$MgAl_2O_4$. From these images, a highly uniform size distribution is observed for both catalysts. The cluster size distribution was determined counting ~150 clusters and it confirmed that the distribution shown in Figure 2 is uniform for the supported Rh and Ir catalysts. However, one can see in Figure 2 that the Rh clusters are slightly bigger than those for Ir. The Rh and Ir cluster sizes are equal to 2.1 and 1 nm (see Table 1), respectively. For both catalysts, the metal dispersion was calculated from the cluster sizes and the results are presented in Table 1. The Ir appears to be very well dispersed on the surface of the $MgAl_2O_4$ support as the dispersion is estimated to be 100% based on the cluster size of 1 nm. Bartholomew and Farrauto[41] stated that it is physically reasonable to predict that a 1.1 nm Pt crystallite will have all atoms exposed. By extension, the estimation of 100% dispersion of Ir is also physically reasonable. For the 5% Rh/$MgAl_2O_4$, the dispersion is lower and estimated to be 48%. It should be noted that the STEM images recorded after reactivity measurements did not reveal noticeable sintering for either catalyst.

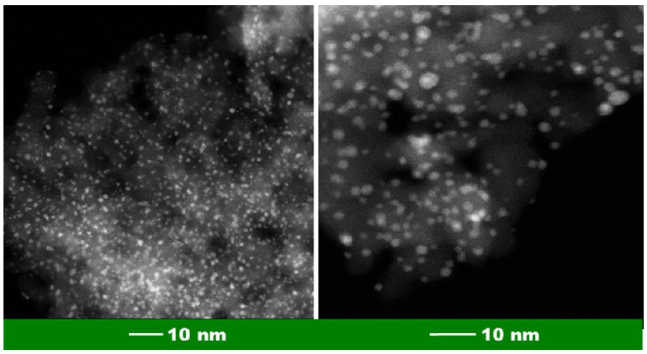

Figure 1. STEM images for the (a) 5% Ir/$MgAl_2O_4$ and (b) 5% Rh/$MgAl_2O_4$ catalysts after exposure to reducing conditions at 850 °C (2 h, 10% H_2/He).

4.1.2. Experimental Catalytic Performance. The catalytic performance for benzene steam reforming at 700 °C is presented in Figure 3 for the 5% Rh/$MgAl_2O_4$ and 5% Ir/$MgAl_2O_4$ catalysts. In Figure 3a, results are presented when H_2O feed concentration was varied while holding the benzene concentration constant at 0.5 mol %. Above a concentration of 35 mol % H_2O in the feed, the benzene conversion was similar for a given catalyst. This weak dependence on steam concentration suggests benzene conversion is not limited by steam above 35 mol % H_2O. We do note a strong dependence on the conversion rate of benzene between 0 and 35 mol % H_2O. These experimental results suggest the earlier stated mechanistic assumption that benzene decomposition is limited by the first C–C bond breaking and ring-opening steps is only valid provided a minimum steam concentration. In this case the minimum steam concentration was experimentally determined to be 35 mol % H_2O, which is equivalent to a steam-to-carbon molar ratio of 12.

Similar to the effect of the steam concentration on the rate of benzene conversion, the effect of varying the benzene concentration while holding the water concentration constant at 35 mol % was investigated. The results are presented in Figure 3b. As the benzene feed concentration increases, the benzene conversion drops. However, the benzene consumption rate (as measured in sccm benzene) remains in a narrow range at approximately 2 sccm. This suggests that benzene adsorption on the catalyst surface is likely not rate limiting.[8]

The Rh catalyst was more active for benzene steam reforming in spite of the fact the Rh catalyst contained larger metallic crystals as illustrated in Figure 2. At 700 °C, the benzene turnover rate, which accounts for the difference in metal dispersions, is greater for the supported Rh catalyst as compared to the Ir catalyst. The turnover rate is approximately 74 mol/mol/min for the 5% Rh/$MgAl_2O_4$ catalyst and 42 mol/mol/min for the 5% Ir/$MgAl_2O_4$ catalyst (Table 1). As illustrated in Figure 4, as the temperature increases from 700 to 850 °C, the activity increases and the benzene conversion is almost complete at 850 °C. Note that in the entire temperature range evaluated in this work, benzene is transformed into H_2, CO, and CO_2. These results demonstrate the greater activity of the Rh catalyst compared to the Ir catalyst for benzene conversion despite the larger cluster size of the Rh metal crystallites. Explanation for the difference in activity between the two metals and understanding the relationship of metal cluster size with benzene conversion are the basis for the theoretical studies described below.

4.2. Theoretical Studies of Adsorption and Decomposition of Benzene on Rh(111) and Ir(111). *4.2.1. Benzene Adsorption on Rh(111) and Ir(111).* We first studied the benzene adsorption on the Rh(111) and the Ir(111) surfaces. The optimized geometric parameters of adsorption configurations are listed in Table 2. Similar to previous DFT results on Pt(111), Pd(111), and Rh(111) surfaces,[15−18,20,23] benzene preferentially adsorbs at two distinguishable sites on the

dx.doi.org/10.1021/cs4000427 | ACS Catal. 2013, 3, 1133−1143

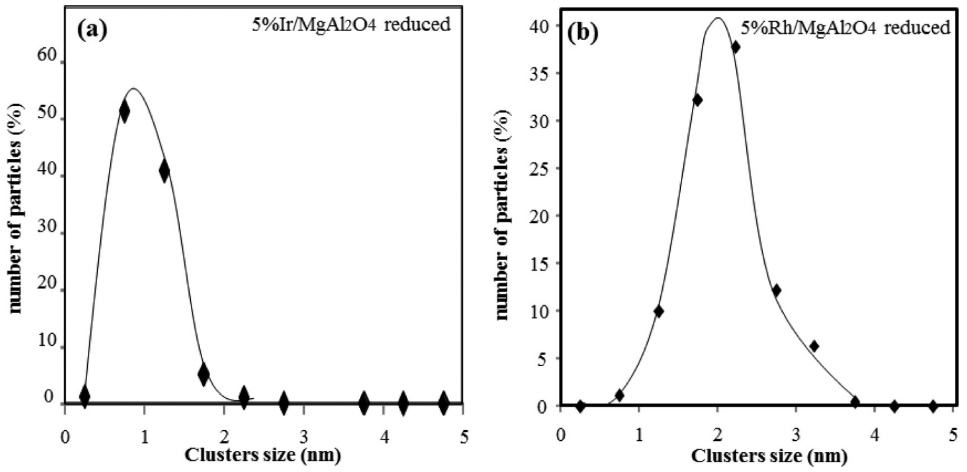

Figure 2. Metal cluster size distribution for the STEM images shown in Figure 1 for (a) 5% $Ir/MgAl_2O_4$ and (b) 5% $Rh/MgAl_2O_4$ catalysts after exposure to reducing conditions at 850 °C (2 h, 10% H_2/He).

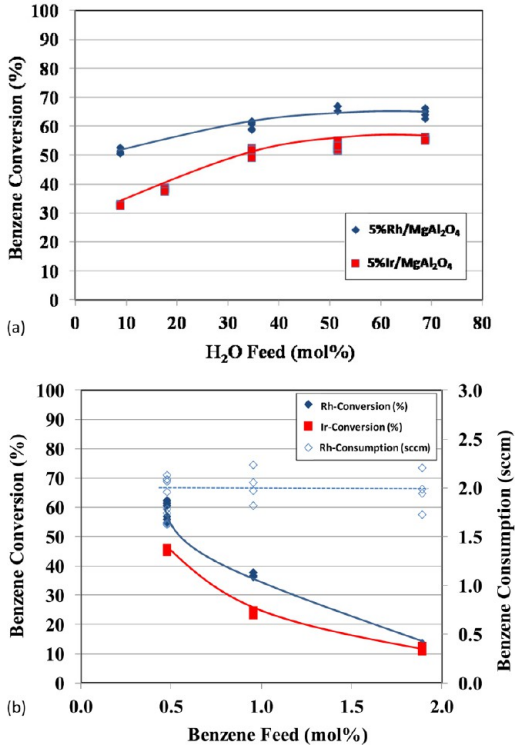

Figure 3. Benzene conversion as a function of (a) H_2O molar feed concentration (0.5 mol % C_6H_6) and (b) benzene molar feed concentration (34.6 mol % H_2O) [T = 700 °C, P = 1 atm, GHSV = 220 000 h^{-1}].

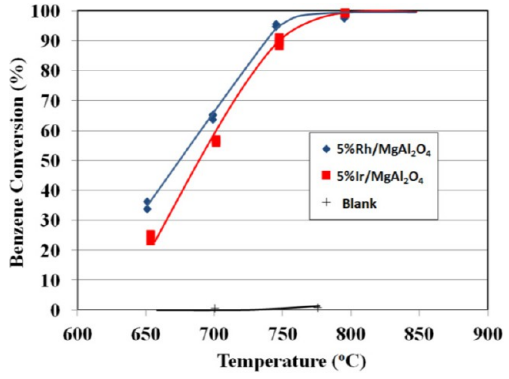

Figure 4. Benzene conversion as a function of temperature (T = 700–850 °C) at P = 1 atm, GHSV = 220 000 h^{-1}, Feed = 64.9% N_2, 34.6% H_2O, 0.5% C_6H_6 (molar).

Rh(111) and the Ir(111) surfaces in the (ring) parallel configuration. In the first adsorption structure, benzene adsorbs at the bridge site (denoted bri30, see Figure 5), with the ring center of the adsorbed benzene located at the bridge site with the C–C bond orientation having a 30° angle with the surface metal–metal bond. In the second adsorption configuration, the ring center of benzene is at the 3-fold hollow (hcp0) site. The calculations suggest that the benzene adsorption at the bri30 site (−1.45 eV) is slightly more favorable than the hcp0 site (−1.32 eV) on Rh(111), consistent with previously reported numbers, −1.53 and −1.51 eV respectively.[16] The calculated C–C and Rh–C bond lengths in the optimized benzene structures at the bri30 site are also in excellent agreement with the previous results of 1.43–1.48 and 2.20 Å.[16]

The calculated adsorption energies of benzene at the bri30 and the hcp0 sites on the Ir(111) surface are −1.19 and −0.98 eV, respectively. Although there is no DFT data of benzene on Ir(111) available, our results are in good agreement with the available experimental values of −1.21 and −1.10 eV.[12] Compared to benzene adsorption on the Rh(111) surface, benzene adsorption on Ir(111) surface is slightly weaker by ∼0.2 eV. This adsorption strength difference explains previous experimental observations that ∼45% benzene molecules desorb from the Ir(111) surface before its decomposition which occurs at 400 K whereas only ∼15% of adsorbed benzene molecules desorb from the Rh(111) surface.[11,12]

By partitioning the adsorption energy of benzene into three components, Morin et al. tried to analyze the different adsorption energies of benzene on the bri30 and hcp0 sites, as well as on the different metal surfaces in terms of geometric distortion and electronic interaction.[16] We note that the distortion energy of the adsorbed benzene molecule in terms of the geometric deformation, such as the C–C bond variations, plays an important role in the interaction between benzene and the metal surface. As shown in Table 2, the stronger adsorption on the Rh(111) surface than the Ir(111) surface, as well as the stronger adsorption at the bri30 site can be partly explained by

dx.doi.org/10.1021/cs4000427 | ACS Catal. 2013, 3, 1133–1143

Table 2. DFT Calculated Binding Energies and Geometric Parameters of Adsorbed Benzene, Phenyl and Chainlike C_6H_6 (c-C_6H_6) on the Periodic Rh(111) and the Ir(111) Surfaces

species	site		Rh(111)	Ir(111)
benzene	bri30	E_{ad} (eV)	−1.45	−1.19
		d(M−C)[c] (Å)	2.21−2.22	2.19−2.21
		d(C−H) (Å)	1.09−1.17, 1.11[b]	1.08−1.11, 1.09[b]
		d(C−C) (Å)	1.43−1.48, 1.43[b]	1.43−1.47, 1,46[b]
	hcp0	E_{ad} (eV)	−1.32	−0.98
		d(M−C)[c] (Å)	2.20−2.22	2.19−2.21
		d(C−H) (Å)	1.09−1.09	1.09−1.09
		d(C−C) (Å)	1.43−1.46	1.43−1.47
phenyl	bri30	E_{ad} (eV)	−3.24	−2.66
		d(M−C)[c] (Å)	2.13−2.20	1.97−2.22
		d(C−H) (Å)	1.09−1.09, 2.93[b]	1.09−1.15, 3.02[b]
		d(C−C) (Å)	1.43−1.459	1.43−1.48
		d(C−H) TS (Å)	1.69[b]	1.88[b]
c-C_6H_6	bri30	E_{ad} (eV)[a]	−0.52	−0.51
		d(M−C)[c] (Å)	2.02−2.21	2.09−2.23
		d(C−H) (Å)	1.09−1.11	1.09−1.10
		d(C−C) (Å)	1.43−1.46, 2.87[b]	1.43−1.46, 2.93[b]
		d(C−C) TS (Å)	2.05[b]	2.05[b]

[a]The adsorption energy of c-C_6H_6 is referenced to the gas-phase benzene. [b]The bond distances at the initial states (IS), the transition states (TS), and the final states (FS). [c]M indicates the metal atom (Rh or Ir)

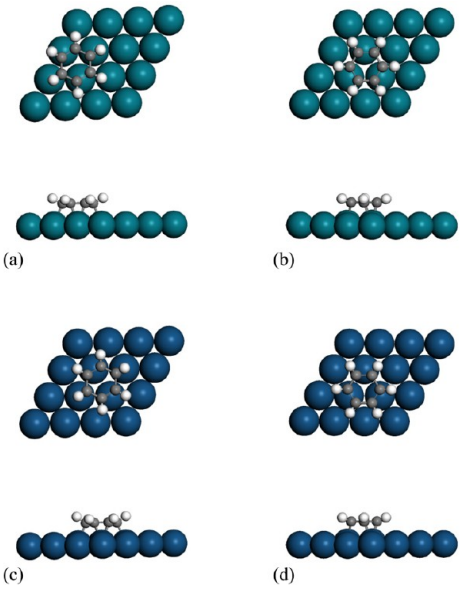

Figure 5. Optimized adsorption structures of benzene on the Rh(111) and the Ir(111) surfaces. (a) bri30 configuration/Rh(111); (b) hcp0 configuration/Rh(111); (c) bri30 configuration/Ir(111); (d) hcp0 configuration/Ir(111). Rh atoms are in dark green; Ir atoms are in blue; H atoms are in white; and C atoms are in gray.

the larger variations of the C−C bond lengths of the adsorbed benzene at the bri30 site on the Rh(111) surface.

4.2.2. Bond Scission of Benzene on Rh(111). The initial decomposition of the adsorbed benzene proceeds via either the dehydrogenation pathway (C−H bond-breaking) leading to phenyl (C_6H_5) formation, or the ring-opening pathway (the C−C bond-breaking) leading to chain-like (c-C_6H_6) alkene species. Beginning with the most stable adsorption structure at the bri30 site, it is found that both C−H and C−C bond scissions of benzene on the Rh(111) surface are highly endothermic. The calculated activation barriers of the C−H bond-breaking and the C−C bond-breaking of benzene on Rh(111) are 1.61 and 1.58 eV, respectively, indicating these two bond scission steps are competitive on the Rh(111) surface. As shown in Figure 6a, the ring structure is slightly rotated when the C−C bond is breaking. At the transition state, all C atoms of the ring bind at the bridge sites with the broken C−C bond distance of 2.05 Å in the final state, the C atoms of

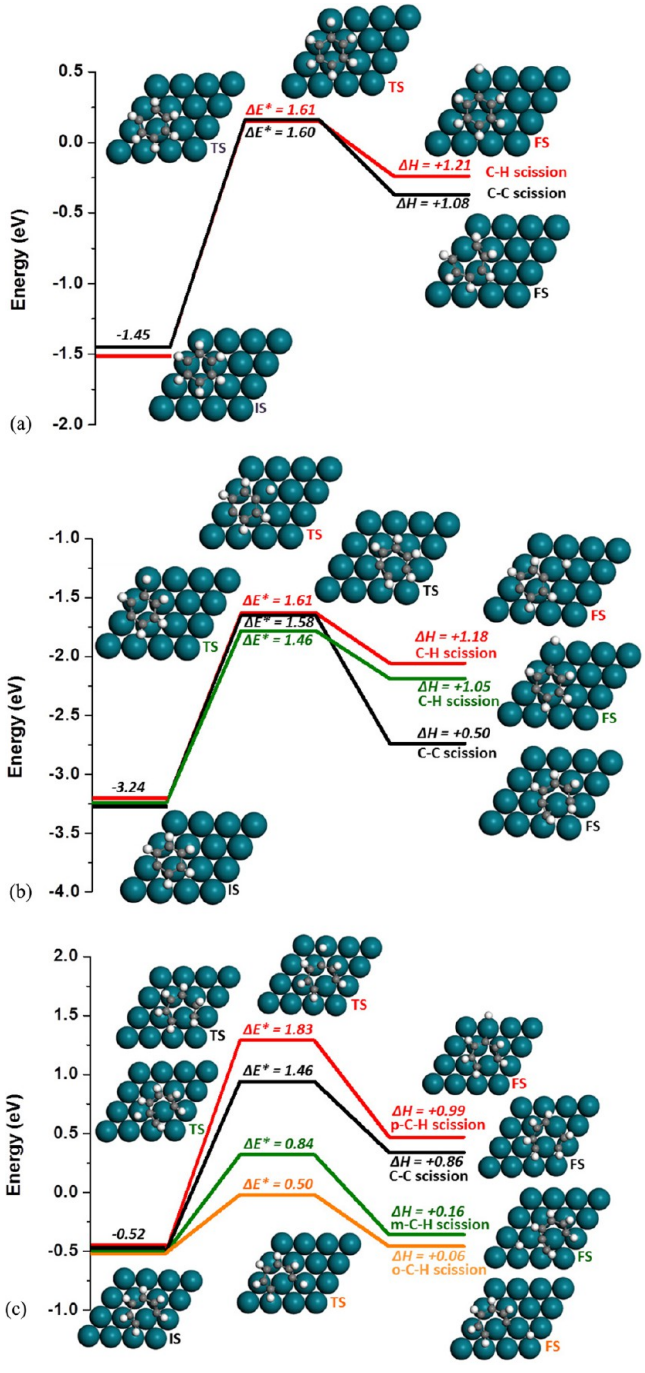

Figure 6. Initial bond scissions for benzene decomposition reaction on the Rh(111) surface. (a) C−H and C−C bond scissions of benzene; (b) C−H and C−C bond scissions of phenyl; (c) C−H and C−C bond scissions of chain-like C_6H_6.

dx.doi.org/10.1021/cs4000427 | ACS Catal. 2013, 3, 1133−1143

the benzene ring have readjusted to each other, resulting in a pair of C atoms bound to one surface Rh atom with a C−C bond length of 1.43−1.46 Å. The C−C bond lengths of c-C_6H_6 are slightly shorter than the C−C bond lengths of the adsorbed benzene.

For the dehydrogenation path of benzene, one of H atom breaks away from the C atom of the ring by moving to the atop site at the transition state, and eventually settling at the bridge site in the final state. Unlike the C−C bond breaking, the ring structure is much less distorted. To find out whether there is a site effect on the benzene decomposition over Rh(111), the C−C bond scission of the adsorbed benzene starting from the hcp0 site was also explored. The calculated reaction energy and activation barrier of the ring-opening step are +0.65 and 1.57 eV, respectively. This is essentially the same as the bri30 site. In conclusion, the first steps of benzene decomposition on the Rh(111) surface involve two competitive C−H and C−C bond scissions leading to phenyl and c-C_6H_6 species.

We further examined the C−H and the C−C bond scissions of the phenyl and the c-C_6H_6 species. For the C−H bond scission of phenyl, three C−H bond scissions with different carbon atom positions (C2, C3, and C4), leading to ortho-, meta- and para-benzyne (C_6H_4) species. Figure 6b shows two C−H bond scission paths leading to the meta-C_6H_4 and the para-C_6H_4. Although the reaction energies are very close, the formation of the meta-C_6H_4 species seems to be slightly favorable over the para-C_6H_4 species because of the lower barrier (1.46 vs 1.61 eV). On the other hand, our calculation shows the C−C bond-breaking of the phenyl is nearly the same as the C−C bond breaking of benzene. The activation barrier for the C−C bond breaking of the phenyl is 1.58 eV, which is very close to the value of 1.60 eV for the benzene although this C−C bond breaking of the phenyl step is slightly less endothermic (+0.50 eV).

The C−H bond-breaking preference order of ortho > meta > para on Rh(111) is also valid for the open-ring c-C_6H_6 species. This is clearly demonstrated by our calculated activation for three C−H bond scissions of the c-C_6H_6 species. The barrier for the ortho−C-H bond breaking is only 0.50 eV, which is lower than the barrier of 0.83 eV for the meta−C-H breaking and dramatically lower than the barrier of 1.84 eV for the para−C-H bond breaking. This trend also corresponds to the decreasing endothermocity order of ortho > meta > para.

The C−C bond scission of the c-C_6H_6 produces a chain-like C_4H_4 species and acetylene (C_2H_2) on the Rh(111) surface. As shown in Figure 6c, the C−C bond between C2 and C3 breaks by the C_2H_2 fragment moving away from the moiety of C_4H_4 species. At the transition state, the C_4H_4 species stays at the bri30 site while the C_2H_2 fragment binds at the hcp0 site at the transition state. The C−C bond is already broken with a C2−C3 distance of 2.05 Å at the transition state. In the final state, the C_2H_2 fragment moves to the bri30 site. Our calculation shows the activation barrier for this C−C bond-breaking path is 1.46 eV with a reaction energy of +0.86 eV. Compared to the ortho- or meta−C-H bond scissions, the C−C bond breaking of the c-C_6H_6 is thermodynamically and kinetically unfavorable. As a result, the further decomposition of the open-ring c-C_6H_6 is most likely to proceed via the ortho- or meta−C-H bonds scissions instead of the C−C and para−C-H bond scissions.

Benzene decomposition on Rh(111) had been studied using TPD, HREELS, and LEED techniques.[11] On the basis of the evidence of the decomposition products of CH and C_2H species, which is the same as the products from acetylene decomposition, Koel et al. proposed that the benzene decomposition begins with the C−C bond scission.[11] However, our DFT results suggest that the C−H and the C−C bond scission pathways of benzene are competitive on the Rh(111) surface, at least for the very first bond-breaking step. Once the ring structure of benzene is open, the C−H bond sessions are kinetically more favorable. We believe that benzene decomposition is very complex, and might go through numerous reaction pathways via the C−C and the C−H bond scissions; it is premature to argue which bond of benzene will be broken based on the final products. For example, the open-ring C_6H_5 species can further dissociate into C_2H and C_4H_4 via the C−C bond breaking, and C_4H_4 can also further dissociate into a mixture of C_2H and CH fragments. In this work, we are focusing only on the initial decomposition of benzene on the Rh(111) and the Ir(111) surfaces. The complete mechanism network of benzene decomposition will be discussed in future work.

4.2.3. Bond Scissions of Benzene on Ir(111). The initial decomposition pathways of the adsorbed benzene on the Ir(111) surface via the C−H and the C−C bond scission are shown in Figure 7a. For the C−C bond scission, the two C atoms move away from the initial atop-like position to the bridge-like position. The C−C bond is broken at the transition state with the C−C distance of 1.88 Å. At the final state, the two C atoms sit at the neighboring bridge site with the C−C distance of 3.02 Å. Similar to the C−C bond scission of benzene on the Rh(111), the four C atoms of the ring are slightly rotating with the two C atoms involved in the bond-breaking process. In contrast, during C−H bond scission, the ring structure of benzene is nearly undisturbed. The disassociating H atom moves away from the C atom, and eventually binds on the atop site on the Ir(111) surface. At the transition state, the H atom resides in the hollow site with the C−H distance of 1.69 Å. Our calculations show that the C−C bond breaking step is thermodynamically and kinetically more favorable than the C−H bond breaking step. Except for the lower barrier (1.60 eV vs 1.97 eV), the C−C bond breaking of benzene on Ir(111) is much less endothermic (∼1.0 eV) than the C−H bond breaking step, although both bond scission steps are still highly endothermic. This is different from the initial decomposition steps of benzene on Rh(111), where the C−C and the C−H bond breaking steps are very competitive.

The phenyl formed by the C−H bond breaking of benzene further dissociates via the C−C and the C−H bond scissions. Similar to the case of phenyl decomposition on Rh(111), as already discussed above, the para-C−H bond scission of phenyl on the Ir(111) is more difficult than the ortho−C-H and the meta-C−H bond scissions. Figure 7b compares the para-C−H bond scission with the C−C bond scission of phenyl. We found that although the para-C−H bond scission of phenyl leading to the para-C_6H_4 species is endothermic by +0.90 eV, while the C−C bond breaking leading to the open-ring C_6H_5 species is exothermic by −0.37 eV, the para-C−H bond scission is still kinetically more favorable than the C−C bond scission.

Finally, we explored the decomposition of the open-ring c-C_6H_6 species on the Ir(111) surface. Again, we note that the C−H bond scission of is slightly endothermic while the C−C bond scission step is exothermic (Figure 7c). The calculated activation barriers for two bond scissions of the c-C_6H_6 species show the C−H bond scission (1.44 eV) is more facile than the C−C bond scission (1.90 eV). It is worth noting that the C−C

dx.doi.org/10.1021/cs4000427 | ACS Catal. 2013, 3, 1133−1143

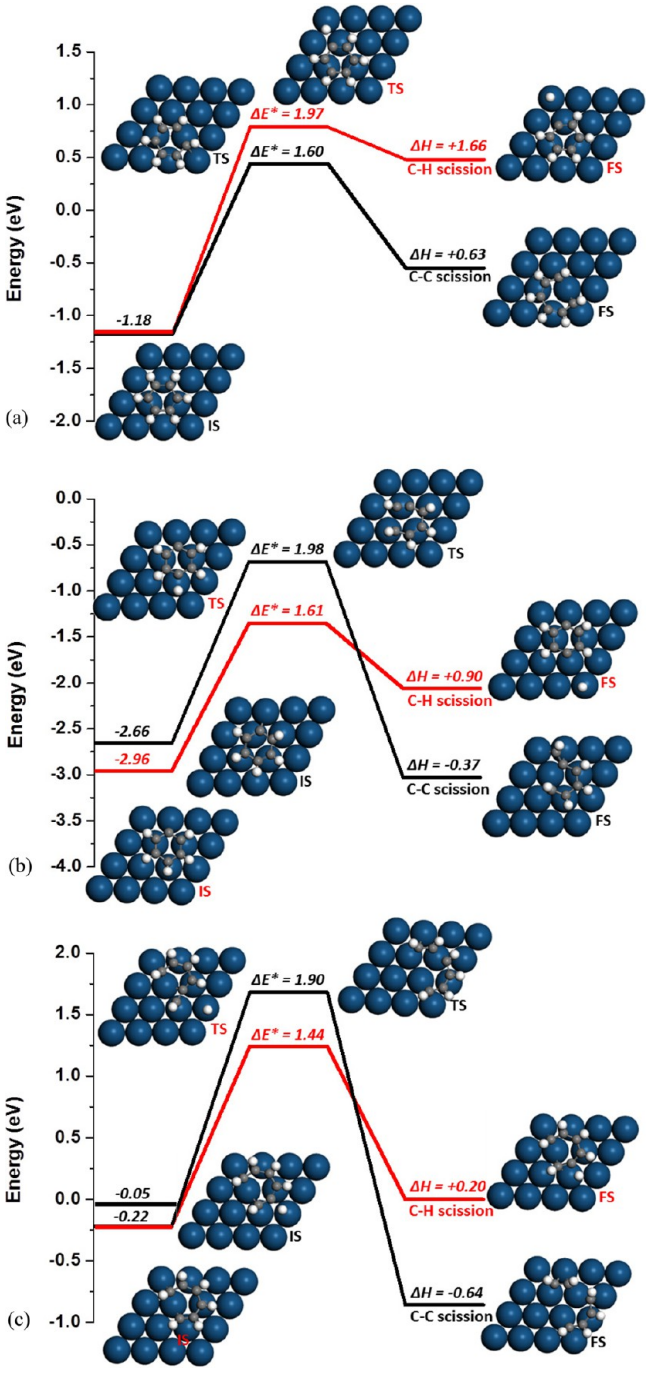

Figure 7. Initial bond scissions for benzene decomposition reaction on the Ir(111) surface. (a) C−H and C−C bond scissions of benzene; (b) C−H and C−C bond scissions of phenyl; (c) C−H and C−C bond scissions of chain-like C_6H_6.

bond scission of the c-C_6H_6 species produces the C_4H_4 species and acetylene on Ir(111).

In summary, we conclude that, unlike the case of the Rh(111) surface, the initial decomposition of benzene on Ir(111) is likely to begin with a C−C bond scission followed by a C−H bond scission rather than a second consecutive C−C bond scission step.

4.3. Initial Decomposition of Benzene on Rh and Ir Clusters. Instead of using a well-defined highly symmetrical cluster, a fully relaxed ∼1 nm Rh_{50} and Ir_{50} clusters, obtained by ab initio molecular dynamics simulations (as described above, were used as the model catalyst particles for the small Rh and Ir catalysts supported on the $MgAl_2O_4$. Since our results suggest that, the initial steps in the activation are likely the most kinetically difficult and ultimately will determine the decomposition route, here we only focus upon the very first C−C or C−H bond scissions of adsorbed benzene on the Rh_{50} and Ir_{50} clusters. Because of the amorphous nature of the equilibrated Rh_{50} cluster, the possible active sites available to the benzene adsorption are numerous. A complete examination of all benzene adsorption possibilities on this small cluster is computationally expensive. To compare with the DFT results over the periodic (111) surfaces presented in the last section, we chose a "quasi-bri30" adsorption configuration of benzene on both Rh_{50} and Ir_{50} clusters, closely resembling the most stable bri30 adsorption site on the (111) surfaces. This allows us to examine the effect of finite cluster size without including the extra complexity of a wide variety of reaction sites.

4.3.1. Rh_{50}. Benzene binds at the pseudo-bri30 site of the (111)-like Rh_{50} cluster surface facet with an adsorption energy of −1.64 eV, suggesting that the benzene adsorption on the Rh_{50} cluster is slightly stronger (by 0.19 eV) than on the Rh(111) surface. The calculated adsorption structure parameters of the adsorbed benzene on the Rh_{50} cluster are given in Table 3. Compared to the C−H and C−C bond lengths of benzene in gas phase (1.09 and 1.40 Å, respectively), we found that both C−H and C−C bond lengths of benzene are slightly extended after adsorption. Starting from this stable adsorption configuration, two initial (very first) dissociation paths of benzene via the C−H and the C−C scissions were examined. As shown in Figure 8a, the activation barriers for the C−H and the C−C scissions are 1.34 and 1.26 eV, respectively. This indicates that two dissociation paths of benzene on the Rh_{50} cluster are competitive, similar to the Rh(111) surface.

Table 3. DFT Calculated Binding Energies and Geometric Parameters of Adsorbed Benzene, Phenyl, and Chain-like C_6H_6 (c-C_6H_6) on the Rh_{50} and the Ir_{50} Clusters

species		Rh_{50}	Ir_{50}
benzene	E_{ad} (eV)	−1.64	−1.78
	d(M−C)[c] (Å)	2.13−2.26	2.12−2.20
	d(C−H) (Å)	1.09−1.13, 1.09[b]	1.09−1.09, 1.09[b]
	d(C−C) (Å)	1.43−1.48, 1.44[b]	1.43−1.49, 1.44[b]
phenyl	E_{ad} (eV)	−4.28	−2.74
	d(M−C)[c] (Å)	2.05−2.21	1.90−2.28
	d(C−H) (Å)	1.09−1.10, 2.73[b]	1.09−1.12, 4.92[b]
	d(C−C) (Å)	1.43−1.49	1.37−1.50
	d(C−H)−TS (Å)	2.07[c]	3.41[c]
c-C_6H_6	E_{ad} (eV)[a]	−0.52[a]	−0.51[a]
	d(M−C)[c] (Å)	1.97−2.22	2.05−2.26
	d(C−H) (Å)	1.09−1.11	1.09−1.21
	d(C−C) (Å)	1.42−1.47, 3.76[b]	1.42−1.48, 2.94[b]
	d(C−C)−TS (Å)	3.29[b]	2.33[b]

[a]The adsorption energy of c-C_6H_6 is referenced to the gas-phase benzene. [b]The bond distances at the initial states (IS), the transition states (TS), and the final states (FS). [c]M indicates the metal atom (Rh or Ir)

Starting from this stable adsorption configuration, two initial (very first) dissociation paths of benzene via the C−H and the C−C scissions were examined. As shown in Figure 8a, the activation barriers for the C−H and the C−C scissions are 1.34 and 1.26 eV, respectively. This indicates that two dissociation paths of benzene on the Rh_{50} cluster are competitive, similar to the Rh(111) surface.

4.3.2. Ir_{50}. The calculated adsorption energy of benzene at the pseudo-bri30 site on the Ir_{50} cluster surface is −1.78 eV. Compared to the Ir(111) surface, benzene adsorption on the small Ir_{50} cluster is much stronger. The optimized structure parameters of the adsorbed benzene on Ir_{50} suggest that only

dx.doi.org/10.1021/cs4000427 | ACS Catal. 2013, 3, 1133−1143

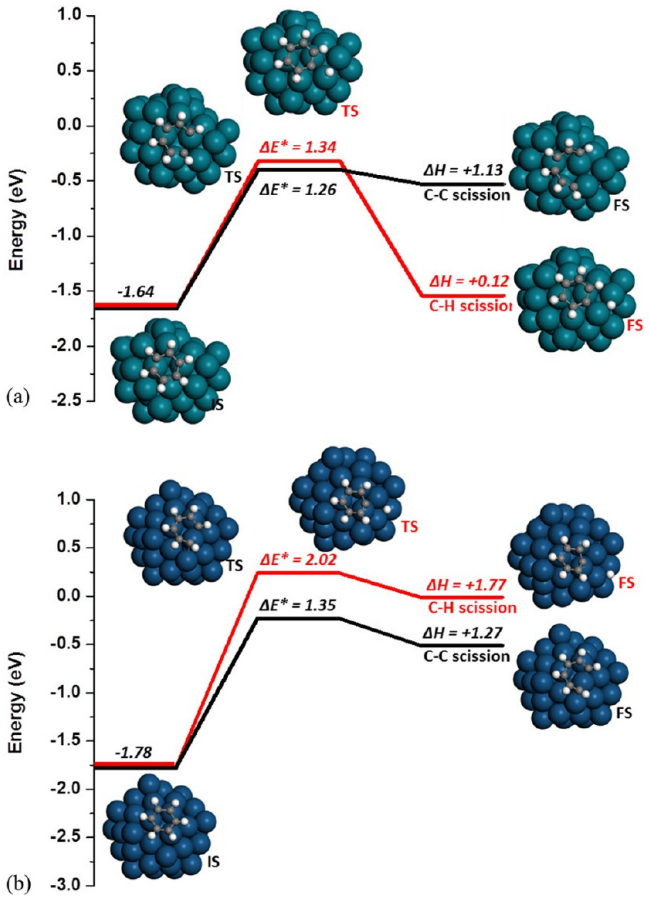

Figure 8. C−C and C−H bond-breaking of benzene on the small (a) Rh_{50} and (b) Ir_{50} clusters.

the C−C bonds of benzene are elongated to 1.43−1.49 Å, while all the C−H bonds is undistorted. Upon adsorption, the benzene dissociation preferentially proceeds via the C−C bond breaking rather than the C−H bond breaking on the Ir_{50} cluster. As shown in Figure 8b, the activation barrier of C−C bond breaking is 1.35 eV, which is much lower than the activation barrier of 2.02 eV for the C−H bond breaking. Our calculations also suggest that both C−C and C−H bond scissions of the adsorbed benzene on the Ir_{50} cluster are highly endothermic, implying the reverse reactions such as the C−C recombination step and hydrogenation step are facile and statistically possible. The C−C recombination step for the open-ring (chain-like) C_6H_6 conversion to benzene is only 0.08 eV.

4.4. General Discussion. A series of DFT calculations of benzene decomposition over Rh and Ir catalysts with two different model surfaces were carried out in this work. The major purpose of the computational modeling is to gain fundamental insights into benzene steam reforming over supported transition metal catalysts. On one hand, we are trying to understand why the supported Rh catalyst is more active than the Ir catalyst. On the other hand, we want to understand the particle size effects on the activity of BSR supported catalysts because sintering and coking are two common issues for tar steam reforming using metal catalysts.[2,3,42−44] It is noteworthy that minimal coking and deactivation were observed in our BSR experiments over the spinel supported Rh and Ir catalysts. The major products from the BSR reaction are H_2, CO, and CO_2, suggesting that the hydrocarbon species, especially the carbon or CH (or C_2H) fragments have been fully oxidized into CO either by the recombination of C and O, or through the HCO route over the two metal particles. As discussed in the section 4.1.2, the benzene conversion becomes nearly constant when the steam-to-carbon ration is above 12. This implies that the benzene decomposition rather than the CO formation or water activation is the rate-determining step in BSR over spinel supported Rh and Ir catalysts. This is also supported by our calculations of water dissociation on small Ir_{50} and Rh_{50} clusters, as well as large Ir and Rh catalysts. We find that the activation barriers for water dissociation are only 0.72 and 0.67 eV on Ir_{50} and Rh_{50} clusters, respectively. Although water activation on both Ir_{50} and Rh_{50} clusters are still endothermic (+0.25 eV), the barriers are slightly lower their corresponding barriers on the (111) surfaces (0.80 and 0.94 eV). Furthermore, the activation barriers for the O−H bond scission of the formed hydroxyl species are calculated as 0.76 and 0.96 eV on the Ir_{50} and the Rh_{50} clusters, which are much lower than the barriers of benzene decomposition. Therefore, we believe that the BSR activity measured in this work is largely dependent upon the benzene decomposition behavior over the supported Rh and Ir catalysts.

Both conversion and turnover rate of BSR on the Rh catalyst are higher than on the Ir catalyst. Our STEM images shown in Figure 1 indicate that the sizes of the spinel supported Rh and Ir particles are about 1 nm, with the narrow size distributions. To comply with experiments, a metal cluster of 50-atoms with a diameter of 1.0 nm was also employed for theoretical mechanistic studies. The size of this equilibrated metal nanocluster used in the calculations is very similar to the one on the spinel support experimentally. As shown in Figure 8, the C−H bond scission of benzene over the small Rh_{50} cluster is thermodynamically neutral (+0.12 eV) while the C−C bond scission over the Rh_{50} cluster and both C−C and C−H bond scissions over the Ir_{50} cluster are highly endothermic (>+1.1 eV). Not only are the activation barriers for the C−C and the C−H bond scissions on the Rh_{50} cluster comparable, the C−C bond recombination (the reverse process for the C−C scission) is also very facile due to the low barrier of 0.21 eV. Similarly, the hydrogenation of phenyl on the Ir_{50} cluster is also very fast because of the extremely low barrier of 0.08 eV. Therefore, we can conclude that the benzene decomposition very likely begins with the C−H bond scission of benzene on the Rh_{50} cluster. The relatively facile benzene decomposition on the Rh_{50} cluster over the Ir_{50} cluster is the underlying reason for the higher BSR activity on the spinel supported Rh catalyst.

Compared to the Rh_{50} cluster, the activation barriers for the C−H and C−C bond scissions of benzene on the Rh(111) surface are higher. This suggests that the increasing particle size will decrease the activity of BSR on Rh catalysts. On the other hand, with increasing particle size, the barrier for the C−C bond scission of benzene increases from 1.35 eV on the Ir_{50} cluster to 1.60 eV on the Ir(111) surface while the barrier for the C−H bond scission are nearly the same on the Ir_{50} cluster and the Ir(111) surface. This indicates that the particle size only affects the C−C bond breaking of benzene, which is the initial step for benzene decomposition on the Ir catalysts. Moreover, we found that the C−C bond-breaking step is much less endothermic on the Ir(111) surface than it on the Ir_{50} cluster. This makes the C−C bond scission of benzene more feasible on the larger Ir catalysts.

dx.doi.org/10.1021/cs4000427 | ACS Catal. 2013, 3, 1133−1143

A kinetic reaction rate analysis was also conducted to shed light on the intrinsic reactivity of Rh and Ir based catalysts. Our results show that the very first step of benzene decomposition in terms of either C−H or C−C bond scission will play the essential role in determining the entire BSR reaction rate. This is because, compared to subsequent decomposition steps, the very first step of benzene decomposition are highly endothermic on both Rh and Ir catalysts irrespective of the particle size. A simple activity index based on the ratio of the decomposition and desorption reaction rate can be defined as

$$\text{activity index} = \frac{r_{\text{decomposition}}}{r_{\text{desorption}}} = \frac{(10^{13})\exp(\Delta E^{\text{act}}/k_{\text{B}}T)}{(10^{13})\exp(\Delta E^{\text{des}}/k_{\text{B}}T)} \quad (6)$$

where ΔE^{act} is the lowest activation barrier of the very first bond scission (C−H or C−C) of the adsorbed benzene molecule; ΔE^{des} is the desorption energy (equivalent of the negative value of the adsorption energy for benzene). By this definition, the larger the activity index, the more active the catalyst for BSR reaction will be.

The activity indexes for large Rh and Ir catalyst particles (using values obtained with Rh(111) and Ir(111) surface models) were calculated as 0.1670 and 0.0067, respectively, at 700 °C. This suggests that the larger Rh catalyst particles are about 25 times more active than their corresponding Ir analogues. In comparison the bulk (111) surfaces show C−C and C−H bond activation energies which are higher than the desorption energy of benzene whereas these events are competitive with desorption on the 1 nm particle implying a higher activity of the smaller particles. The activity indexes for small Rh and Ir catalyst particles (Rh_{50} and Ir_{50} clusters) are 93.0 and 177.0, respectively, implying the BSR activity on the small Ir particle can be almost twice as active as its counterpart small Rh catalyst. However, we also note that the C−H bond scission of the adsorbed benzene on the Ir cluster is highly endothermic although the barrier is low. This indicates that the reverse reaction path, that is, the C−H recombination for benzene formation, is very facile. If we take both thermodynamic and kinetic factors into account, it is expected that the activity of BSR on the small supported Rh and Ir catalysts are very comparable. Considering that the larger supported Rh catalyst is pronouncedly more active than the larger Ir catalyst, it is reasonable to conclude that the spinel supported Rh, where the majority of catalyst particles was found to be highly dispersed small particles, is slightly more active than the spinel supported Ir catalysts for BSR reaction. This is consistent with our experimental observation that the turnover frequency of BSR on the $Rh/MgAl_2O_4$ is only two times higher than on the $Ir/MgAl_2O_4$ under high dispersion condition.

5. CONCLUSIONS

In the present work, the catalytic reactivity of benzene steam reforming over spinel-supported Rh and Ir catalysts was investigated using a combination of experimental measurements and first-principles density functional theory calculations. For each supported metal catalyst, two kinds of catalyst models were considered to represent the metal catalyst at different dispersions. The larger supported metal catalysts at low dispersion were modeled as a periodic (111) surface, while smaller supported metal catalysts under higher dispersion were modeled by nanometer-sized metal clusters. We also investigated the effects of water and benzene concentrations in the feed on the benzene conversion. When the steam-to-carbon ratio is above 12, the weak dependence of water concentration on the benzene conversion suggest the activity of BSR on supported Rh and Ir catalysts are not limited by the adsorption but the initial decomposition of benzene. Consistent with our experimental observation that the $Rh/MgAl_2O_4$ catalyst is more active with higher benzene turnover frequency and conversion, our calculations of initial decomposition of benzene over four model surfaces suggest the benzene decomposition is more facile on Rh catalysts. Our results indicate that the C−C and the C−H bond scissions of benzene on the Rh(111) and the Rh_{50} cluster are competitive, while the C−C bond scission is slightly more favorable on the Ir(111) surface and the Ir_{50} cluster. Moreover, our results show that benzene decomposition is kinetically more favorable on the small clusters rather than on the larger particles. Compared to the barriers of ∼1.6 eV for the C−C and the C−H scissions of benzene on the Rh(111) surface, the barriers on the Rh_{50} cluster are lower (∼1.3 eV). In this case, both C−C and C−H bond scissions will be facilitated by decreasing particle size of supported Rh catalysts. However, the particle effects on the initial decomposition of benzene on Ir catalysts are different. The decreasing particle size promotes the C−C bond scission but inhibits the C−H bond scission. This suggests that the benzene decomposition is very complex. The specific bond-breaking step is not only determined by the nature of metal, but also nonmonotonically varied with the particle size (steric effects).

AUTHOR INFORMATION

Corresponding Author

*E-mail: donghai.mei@pnnl.gov (D.M.); robert.dagle@pnnl.gov (R.D.).

Notes

The authors declare no competing financial interest.

ACKNOWLEDGMENTS

This work was financially supported by the United States Department of Energy's Office of Biomass Program's. Computing time was granted by a user project at the Molecular Science Computing Facility in the William R. Wiley Environmental Molecular Sciences Laboratory (EMSL). Part of computational time is provided by the National Energy Research Scientific Computing Center (NERSC). The research was performed at EMSL, a national scientific user facility sponsored by the Department of Energy's Office of Biological and Environmental Research and located at Pacific Northwest National Laboratory (PNNL). We also want to thank Cortland Johnson of PNNL for making the cover graphic.

REFERENCES

(1) Huber, G. W.; Iborra, S.; Corma, A. *Chem. Rev.* **2006**, *106*, 4044.
(2) Abu El-Rub, Z.; Bramer, E. A.; Brem, G. *Ind. Eng. Chem. Res.* **2004**, *43*, 6911.
(3) Yung, M. M.; Jablonski, W. S.; Magrini-Bair, K. A. *Energy Fuels* **2009**, *23*, 1874.
(4) Coll, R.; Salvado, J.; Farriol, X.; Montane, D. *Fuel Process. Technol.* **2001**, *74*, 19.
(5) Torres, W.; Pansare, S. S.; Goodwin, J. G., Jr. *Catal. Rev.: Sci. Eng.* **2007**, *49*, 407.
(6) Tomishige, K.; Miyazawa, T.; Asadullah, M.; Ito, S.; Kunimori, K. *Green Chem.* **2003**, *5*, 399.

(7) Tsyganok, A. I.; Inaba, M.; Tsunoda, T.; Hamakawa, S.; Suzuki, K.; Hayakawa, T. *Catal. Comm.* **2003**, *4*, 493.
(8) Colby, J. L.; Wang, T.; Schmidt, L. D. *Energy Fuels* **2010**, *24*, 1341.
(9) Simell, P. A.; Hakala, N. A. K.; Haario, H. E.; Krause, A. O. I. *Ind. Eng. Chem. Res.* **1997**, *36*, 42.
(10) Rostrup-Nielsen, J. R. *J. Catal.* **1973**, *31*, 173.
(11) Koel, B. E.; Crowell, J. E.; Bent, B. E.; Mate, C. M.; Somorjai, G. A. *J. Phys. Chem.* **1986**, *90*, 2949.
(12) Weststrate, C. J.; Bakker, J. W.; Gluhoi, A. C.; Ludwig, W.; Nieuwenhuys, B. E. *Surf. Sci.* **2007**, *601*, 748.
(13) Tsai, M. C.; Muetterties, E. L. *J. Am. Chem. Soc.* **1982**, *104*, 2534.
(14) Jenkins, S. J. *Proc. R. Soc. A* **2009**, *465*, 2949.
(15) Morin, C.; Simon, D.; Sautet, P. *J. Phys. Chem. B* **2004**, *108*, 12084.
(16) Morin, C.; Simon, D.; Sautet, P. *J. Phys. Chem. B* **2004**, *108*, 5653.
(17) Morin, C.; Simon, D.; Sautet, P. *Surf. Sci.* **2006**, *600*, 1339.
(18) Saeys, M.; Reyniers, M. F.; Marin, G. B.; Neurock, M. *J. Phys. Chem. B* **2002**, *106*, 7489.
(19) Saeys, M.; Reyniers, M. F.; Neurock, M.; Marin, G. B. *J. Phys. Chem. B* **2005**, *109*, 2064.
(20) Saeys, M.; Thybaut, J. W.; Neurock, M.; Marin, G. B. *Mol. Phys.* **2004**, *102*, 267.
(21) Fan, C.; Zhu, Y.-A.; Zhou, X.-G.; Liu, Z.-P. *Catal. Today* **2011**, *160*, 234.
(22) Gao, W.; Zheng, W. T.; Jiang, Q. *J. Chem. Phys.* **2008**, 129.
(23) Saeys, M.; Reyniers, M. F.; Neurock, M.; Marin, G. B. *J. Phys. Chem. B* **2003**, *107*, 3844.
(24) Boudart, M.; Djega-Mariadassou, G. *The Kinetics of Heterogeneous Catalytic Reactions*; Princeton University Press: Princeton, NJ, 1984.
(25) Ramallo-Lopez, M. A.; Requejo, F. G.; Craievich, A. F.; Wei, J.; Avalos-Borja, M.; Iglesia, E. *J. Mol. Catal. A: Chem.* **2005**, *228*, 299.
(26) Kresse, G.; Furthmuller, J. *Phys. Rev. B* **1996**, *54*, 11169.
(27) Kresse, G.; Furthmuller, J. *Comput. Mater. Sci.* **1996**, *6*, 15.
(28) Kresse, G.; Hafner, J. *Phys. Rev. B* **1994**, *49*, 14251.
(29) Blochl, P. E. *Phys. Rev. B* **1994**, *50*, 17953.
(30) Kresse, G.; Joubert, D. *Phys. Rev. B* **1999**, *59*, 1758.
(31) Perdew, J. P.; Chevary, J. A.; Vosko, S. H.; Jackson, K. A.; Pederson, M. R.; Singh, D. J.; Fiolhais, C. *Phys. Rev. B* **1992**, *46*, 6671.
(32) Klimes, J.; Bowler, D. R.; Michaelides, A. *Phys. Rev. B* **2011**, *83*, 195131.
(33) Lippert, G.; Hutter, J.; Parrinello, M. *Mol. Phys.* **1997**, *92*, 477.
(34) VandeVondele, J.; Krack, M.; Mohamed, F.; Parrinello, M.; Chassaing, T.; Hutter, J. *Comput. Phys. Commun.* **2005**, *167*, 103.
(35) Henkelman, G.; Jonsson, H. *J. Chem. Phys.* **1999**, *111*, 7010.
(36) Mei, D.; Karim, A. M.; Wang, Y. *ACS Catal.* **2012**, *2*, 468.
(37) Mei, D. H.; Karim, A. M.; Wang, Y. *J. Phys. Chem. C* **2011**, *115*, 8155.
(38) Mei, D. H.; Xu, L. J.; Henkelman, G. *J. Phys. Chem. C* **2009**, *113*, 4522.
(39) Mei, D. H.; Xu, L.; Henkelman, G. *J. Catal.* **2008**, *258*, 44.
(40) Xu, L. J.; Mei, D. H.; Henkelman, G. *J. Chem. Phys.* **2009**, *131*, 244520.
(41) Bartholomew, C. H.; Farrauto, R. J. *Fundamentals of Industrial Catalytic Processes*, 2nd ed.; John Wiley & Sons, Inc.: Hoboken, NJ, 2006.
(42) Ammendola, P.; Cammisa, E.; Lisi, L.; Ruoppolo, G. *Ind. Eng. Chem. Res.* **2012**, *51*, 7475.
(43) Duprez, D. *Appl. Catal., A* **1992**, *82*, 111.
(44) Duprez, D.; Miloudi, A.; Delahay, G.; Maurel, R. *J. Catal.* **1984**, *90*, 292.